JOURNAL OF PROPULSION AND POWER
Vol. 24, No. 4, July–August 2008

Analytical Computation of Leading-Edge Truncation Effects on Inviscid Busemann-Inlet Performance

Timothy F. O'Brien* and Jesse R. Colville†
Aerojet, Sacramento, California 95813-6000

DOI: 10.2514/1.30178

An approach is presented to analytically predict the conservation-averaged inviscid Busemann-inlet performance properties at the throat, accounting for the effect of leading-edge truncation. A control volume is drawn such that the calculation of throat-inlet performance relies on the accurate prediction of the pressure integral along the surface. The pressure integral is predicted by assuming a leading-edge total pressure loss and a Mach number distribution similar to a nontruncated Busemann inlet. The resulting surface profiles can also be used to predict the bow and terminating shock wave shapes. The pressure-integral-prediction approach is compared with a set of inviscid axisymmetric computational fluid dynamics solutions on the same geometries. The comparisons show that the pressure-integral-prediction approach compares favorably with the computational fluid dynamics solutions for inlets with a moderate contraction ratio and truncation angles no greater than 5 deg.

Nomenclature

A	=	area
CR	=	contraction ratio, A_1/A_2
M	=	Mach number
$\dot{m}$	=	mass flow rate
PR	=	pressure ratio, p_2/p_1
p	=	pressure
R	=	gas constant
T	=	temperature
V	=	velocity
X'	=	nondimensional length
β	=	terminating shock angle
γ	=	ratio of specific heats
δ_{trunc}	=	leading-edge truncation angle
Π	=	total pressure recovery
ρ	=	density
σ^2	=	standard deviation

Subscripts

des	=	design conditions for the truncated Busemann inlet
des, pure	=	design conditions for the pure nontruncated Busemann inlet
LE	=	leading-edge conditions
max	=	maximum started inlet value
pure	=	pure Busemann-inlet performance
surf	=	inlet surface conditions
t	=	total conditions
x	=	frontal area
1	=	freestream conditions
2	=	throat conditions

I. Introduction

THE Busemann-inlet [1] concept has received considerable attention lately as a streamline generator for high-speed, streamline-traced, airbreathing inlet surfaces [2–5]. The Busemann-inlet concept is so named because it was first identified by Busemann [1] as a solution to the Taylor–Maccoll equation [6] for supersonic conical flow. Further, Molder [7] identified two additional solutions to the Taylor–Maccoll equation, which he termed inward conical flow A (ICFA) and inward conical flow B (ICFB).

The theoretical performance of a pure Busemann inlet is readily calculated by numerical integration of the Taylor–Maccoll equation (first published by Molder and Szpiro [8]) or by using small-disturbance theory [9]. The solution for the Busemann-inlet surface yields a flow streamline that can be used to generate three-dimensional streamline-traced inlet geometries. These streamline-traced geometries have been tested both in component form [10] and in an integrated free-jet engine under the supersonic combustion ramjet (SCRAM) missile program [11].

Given the interest in these types of inlet shapes, it is not surprising that numerous computational investigations have been undertaken to quantify the on- and off-design performance of Busemann and streamline-traced Busemann-inlet surfaces (see [12,13] as examples). These studies largely focus on running computational solutions of the inlet flowfield to characterize starting and inlet performance. What is surprising is that once the pure Busemann-inlet shape is modified for engineering application (leading-edge truncation for inlet-length reduction, leading-edge blunting for manufacturability and maintainability, and viscosity), the focus of study was purely computational. No studies have been performed (to the authors' knowledge) to analytically/theoretically describe the modified flowfield and to predict performance with nonideal effects included.

This paper aims to establish a starting point to analytically predict the behavior of nonideal Busemann inlets, by including the effects of leading-edge truncation on the inviscid performance of pure Busemann inlets. Analytical approaches are presented to predict the pressure and Mach number distribution on the modified Busemann geometry, which is sufficient information to calculate throat performance that conserves mass, momentum, and energy (conservation-averaged properties), as well as the bow and terminating shock shapes. The truncated Busemann-inlet shape is generated using the BUSE code [14]. The resulting streamline shape is read into a FORTRAN code that analytically predicts the conservation-averaged performance and shock structure of the truncated inlet design using the current theory. Inviscid computational fluid dynamics (CFD) solutions are performed on the same truncated Busemann-inlet geometries and postprocessed for conservation-averaged performance. Comparisons are then made between the theory and CFD results for both performance and shock shape estimation.

Presented as Paper 26 at the 45th AIAA Aerospace Sciences Meeting and Exhibit, Reno, NV, 8–11 January 2007; received 1 February 2007; accepted for publication 11 February 2008.

*Engineering Specialist, Engineering Analysis, P.O. Box 13222. Senior Member AIAA.
†Engineer, Engineering Analysis, P.O. Box 13222. Member AIAA.

The goal of this approach is a better fundamental understanding of one of the nonideal effects on Busemann-inlet performance: namely, the truncation of the geometry to reduce inlet length. Understanding of the basic physics behind the flow generator should aid in understanding how to design, analyze, and interpret computational and experimental results from future Busemann streamline-traced inlet designs. Although the current approach only addresses the effect of leading-edge truncation, the resulting predictions of the current theory could form the basis for future analytical estimations of the effects of leading-edge blunting and viscosity on performance. Leading-edge effects could be modeled using modified Newtonian flow theory [15] for pressure drag and shock shape correlations, similar to those of Billig [16], for flow over supersonic wedges and cones for bow shock behavior. Viscous effects could be modeled in a manner similar to supersonic wedges, cones, and/or nozzles, using an approach such as the reference-temperature method [17], with the subsequent prediction for viscous drag and momentum thickness used to alter the predicted performance of the inlet.

II. Truncation Approach and Its Effects on the Flowfield

There are two approaches known to the authors to truncate a pure Busemann inlet. The first approach solves for a pure Busemann inlet with a design Mach number $M_{\text{des,pure}}$ and a design contraction ratio $\text{CR}_{\text{des,pure}}$ higher than desired for the truncated inlet. The pure Busemann inlet is then trimmed to the desired truncation angle δ_{trunc}. If $M_{\text{des,pure}}$ and $\text{CR}_{\text{des,pure}}$ are selected correctly, then when the pure Busemann inlet is truncated to δ_{trunc}, the desired design contraction ratio CR_{des} of the truncated inlet is matched. A match for the design Mach number M_{des} of the truncated inlet is found by verifying that the surface Mach number on the truncated inlet corresponds to the Mach number after M_{des} is isentropically turned to δ_{trunc}. An example of a Busemann inlet truncated in this fashion is shown in Fig. 1 (only half of the inlet is shown). The second approach to truncation of a pure Busemann inlet uses the ICFA leading-edge flowfield developed by Molder [7]. ICFA geometries are the theoretically correct shapes to generate a pure conical shock wave off of the leading edge. However, the resulting ICFA extension needed for the desired δ_{trunc}, M_{des}, and CR_{des} results in a longer inlet than with the first truncation approach listed previously. For this paper, the first approach for truncation will be used, but it will be shown in Sec. III that the ICFA flowfield proves to be very useful in predicting the pressure profile on the truncated inlet surface.

Also plotted in Fig. 1 are representative flowfields of the pure Busemann inlet and its truncated counterpart. The pure inviscid Busemann inlet results in a series of linear isobars that focus on the conical axis of rotation (selected to be at coordinate [0, 0] for all inlets in this study). A conical termination shock wave is then formed that turns the flow uniformly back to an axial orientation. This shock wave terminates at the body shoulder of the inlet (selected to be the unit radius for all inlets in this study), which then defines the inlet-throat location. With the addition of truncation, a sharp corner is created at the leading edge of the inlet. The sharp leading-edge corner results in the formation of a curved bow shock that travels toward the centerline. The reflection of the bow shock wave off of the symmetry line occurs beyond the theoretical focus point of the pure Busemann inlet. It is noted that as the bow shock wave approaches the symmetry axis, its shock slope gets steeper, eventually forming a standing normal shock wave near the symmetry axis. Fortunately, the radial height of the normal shock wave is very small for values of truncation angle that are typically investigated ($\delta_{\text{trunc}} \leq 5$ deg). The resulting shock reflection off of the symmetry line subsequently passes through the inlet-throat plane, below the inlet shoulder of the pure Busemann inlet.

The addition of other nonideal effects, such as leading-edge blunting and viscosity, cause the bow shock location to shift in a direction opposite that of the effects of truncation. Leading-edge blunting causes the formation of a normal shock standoff, along with further nonisentropic compression aft of the leading edge due to the influence of characteristic propagation off of the leading edge. These

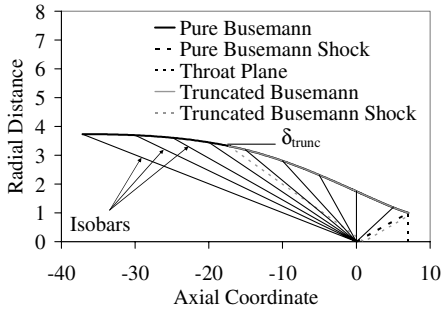

Fig. 1 Example of a pure Busemann inlet and its truncated counterpart (radial axis exaggerated).

phenomena cause the bow shock to move upstream within the inlet. The effect of viscosity adds additional surface inclination to the inlet, through the effects of the displacement thickness, also causing the bow shock to move upstream within the inlet. Although the effects of truncation on inlet performance may be small compared with leading-edge blunting and viscosity, the effects of truncation cannot be ignored when predicting bow shock behavior. Ignoring truncation effects would ultimately result in an overestimate of the upstream movement of the bow shock.

III. Performance Prediction Methodology

A. Governing Equations for Inlet Performance

It is desired to predict the conservation-averaged throat properties of truncated Busemann inlets using the truncation technique discussed in Sec. II. The one-dimensional governing continuity equation (1), axial momentum equation (2), energy equation (3), and state equation (4) for the truncated Busemann inlet are as follows:

$$\rho_1 V_1 A_1 = \rho_2 V_2 A_2 \tag{1}$$

$$p_1 A_1 + \dot{m}_1 V_1 = p_2 A_2 + \dot{m}_2 V_2 + \int_1^2 p_{\text{surf}}\, \mathrm{d}A_x \tag{2}$$

$$T_{t,1} = T_{t,2} \tag{3}$$

$$p = \rho R T \tag{4}$$

where station 1 refers to freestream conditions; station 2 refers to throat conditions; Eq. (2) assumes inviscid flow; Eq. (3) assumes adiabatic walls and a calorically perfect gas; Eq. (4) assumes a perfect gas; and ρ, V, A, p, $\dot{m}$, p_{surf}, A_x, T_t, and T refer to the static density, velocity, cross-sectional area, static pressure, mass flow rate, inlet-wall pressure, inlet-wall frontal area, total temperature, and static temperature, respectively. The desired conservation-averaged inlet performance parameters are the compression ratio $\text{PR} = p_2/p_1$ and the total pressure recovery Π. The compression ratio can be found from substituting Eqs. (3) and (4) into Eq. (1):

$$\text{PR} = \sqrt{\frac{1 + [(\gamma - 1)/2]M_1^2}{1 + [(\gamma - 1)/2]M_2^2}} \frac{M_1}{M_2} \text{CR}_{\text{des}} \tag{5}$$

The total pressure recovery can then be calculated from the isentropic gas relations:

$$\Pi = \text{PR} \left(\frac{1 + [(\gamma - 1)/2]M_2^2}{1 + [(\gamma - 1)/2]M_1^2} \right)^{\frac{\gamma}{\gamma - 1}} \tag{6}$$

With Eqs. (5) and (6), computation of the compression ratio and the total pressure recovery can be performed if the throat Mach number is known. Substituting Eqs. (1) and (5) into Eq. (2) yields the following relationship for the throat Mach number:

$$1+\gamma M_1^2=\sqrt{\frac{1+[(\gamma-1)/2]M_1^2}{1+[(\gamma-1)/2]M_2^2}}\frac{M_1}{M_2}(1+\gamma M_2^2)+\frac{1}{A_1}\int_1^2\frac{p_{\text{surf}}}{p_1}\,\mathrm{d}A_x \tag{7}$$

It is observed from Eq. (7) that if the inlet-wall pressure integral is known, then the throat Mach number can be solved and substituted into Eqs. (5) and (6) to obtain the conservation-averaged throat properties. The next section will discuss how the inlet-wall pressure distribution can be analytically predicted.

B. Analytical Prediction of the Wall Pressure Integral

Prediction of the wall pressure integral on the truncated inlet begins by selecting the leading-edge boundary condition. To accurately model the inlet performance, the total pressure loss caused by the bow shock off of the truncated leading edge must be determined and applied to the surface properties at the leading edge. Through comparison with CFD results (to be subsequently discussed), it was found that the total pressure loss at the leading edge is well approximated by the total pressure loss on a Busemann inlet with an ICFA leading-edge truncation that closes out at the desired δ_{trunc}. An example of an ICFA leading-edge geometry and its resulting surface properties is shown in Fig. 2. The leading-edge surface properties for the truncated inlet are then set to be the surface Mach number and static pressure ratio at the end of the ICFA leading edge.

With the leading-edge properties defined, the next step is to determine the surface distribution for the Mach number and static pressure ratio from the leading edge to the inlet throat. The Mach number distribution on the surface of the truncated inlet is assumed to be the same as that on a pure Busemann inlet of M_{des} and CR_{des}. An example of the change in surface Mach number versus a nondimensional length $[\mathrm{d}M/\mathrm{d}X']$ for a pure Busemann inlet is shown in Fig. 3. A value of $X'=0$ defines the location at which the surface Mach number on the pure Busemann inlet matches the leading-edge boundary condition on the truncated Busemann inlet. A value of $X'=1$ defines the inlet-throat location. The surface Mach number on the truncated inlet, as a function of X', can then be calculated by integrating the Mach number distribution curve from the pure Busemann inlet as follows:

$$M_{\text{surf}}(X')=M_{\text{LE}}+\int_0^{X'}[\mathrm{d}M/\mathrm{d}X']\,\mathrm{d}X' \tag{8}$$

The surface-pressure-ratio distribution can then be calculated by assuming isentropic compression along the truncated Busemann inlet:

$$\frac{P_{\text{surf}}}{P_1}(X')=\frac{P_{\text{LE}}}{P_1}\left(\frac{1+[(\gamma-1)/2]M_1^2}{1+[(\gamma-1)/2][M_{\text{surf}}(X')]^2}\right)^{\frac{\gamma}{\gamma-1}} \tag{9}$$

As will be shown in Sec. V, the preceding process to calculate the Mach number and pressure distribution on the truncated Busemann-inlet surface matches quite well with 2-D axisymmetric CFD results. With the pressure distribution known, the wall pressure integral can then be calculated and input into Eq. (7) to solve for the conservation-averaged throat Mach number. The result of Eq. (7) can then be input into Eqs. (5) and (6) to solve for the remaining desired inlet performance parameters.

C. Analytical Prediction of the Bow and Reflection Shock Shapes

With knowledge of the surface-pressure distribution, a prediction of the bow shock wave and its reflection can be obtained. The overall process to predict the shock shapes is shown in Fig. 4. The basic assumption behind predicting the shock wave shape is to assume that the truncated inlet flowfield is conical about the theoretical shock-reflection point (coordinates [0, 0]). Thus, straight isobars can be traced from every point on the inlet to the theoretical shock-reflection point. The leading-edge shock angle is solved using the pressure ratio at the leading edge and the freestream Mach number. The shock then travels downstream until it intersects the first isobar off of the truncated inlet after the leading edge. The shock angle is increased to match the pressure ratio of the intersecting isobar using the freestream Mach number, then travels further downstream until it intersects the next isobar. In this way, the shock traces down to the last isobar, which comes from the inlet-throat shoulder. Below the last isobar, the shock wave shape is extrapolated to the symmetry axis using a fourth-order fit of all of the predicted shock points upstream of the last isobar. Once the axial location of the shock reflection is found, the reflecting shock wave is assumed to be at the same angle as the last isobar to maintain the conical assumption of the flowfield.

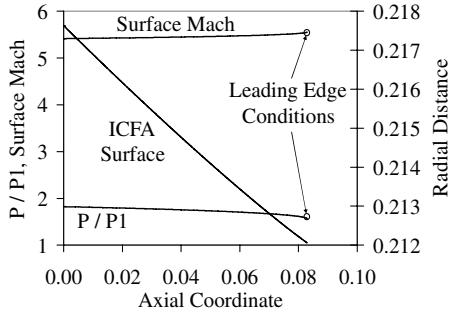

Fig. 2 Example of an ICFA leading-edge and boundary conditions for the truncated leading edge; $M_{\text{des}}=6$, $\delta_{\text{trunc}}=3\,\text{deg}$, and $\gamma=1.4$.

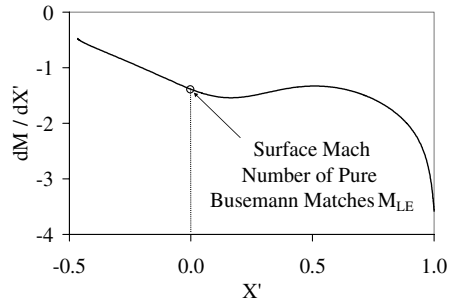

Fig. 3 Mach number distribution on a truncated Busemann from the pure Busemann inlet; $M_{\text{des}}=6$ and $\text{CR}_{\text{des}}=7$.

IV. CFD Undertaken to Validate the Pressure-Integral Approach

A. CFD Methodology

A series of CFD simulations were conducted to validate the theoretical pressure-integral approach. Design-of-experiments methods were employed to reduce the total number of runs and to gather the needed data more efficiently. The design variables were chosen to be freestream Mach number, truncation angle, and contraction ratio. The upper and lower bounds on Mach number and truncation angle were set at 4 and 10 and 1 and 5 deg, respectively. Because the maximum contraction ratio is a function of freestream

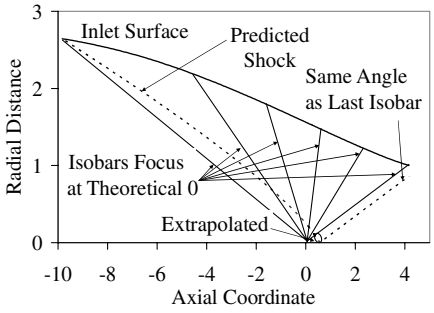

Fig. 4 Theoretical process to predict truncated inlet bow shock wave and reflection shape; $M_{\text{des}}=6$, $\text{CR}_{\text{des}}=7$, and $\delta_{\text{trunc}}=3\,\text{deg}$.

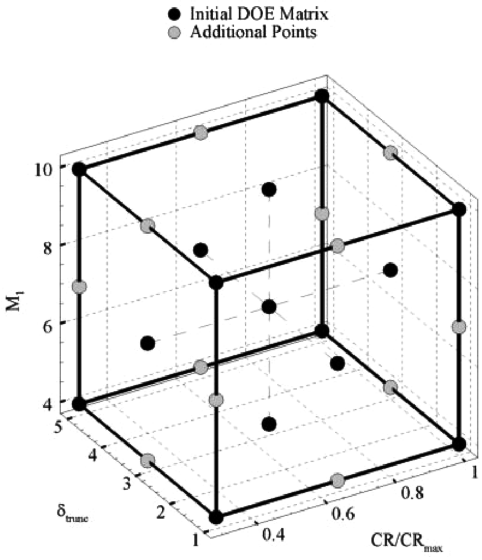

Fig. 5 CFD simulation matrix.

Mach number, the contraction ratio design variable was scaled by CR_{max}; thus, the upper bound on CR/CR_{max} was 1.0. The lower bound was set at 0.3. For the actual CFD, CR_{max} was approximated to be the contraction ratio that would isentropically compress the freestream flow to a throat Mach number equal to half the freestream value [18]:

$$CR_{max} = \sqrt{0.25\left(\frac{1+[(\gamma-1)/2]M_1^2}{1+0.125(\gamma-1)M_1^2}\right)^{\frac{\gamma+1}{\gamma-1}}} \tag{10}$$

The CFD-run matrix was created using the statistical analysis software Minitab, Release 14. The Minitab results are shown in Fig. 5. As displayed, Minitab found that the optimal design space included the eight corners of the design box, the center of the box, and the center point of each face, totaling 15 cases (black points). However, as is subsequently discussed, the simulation times were not long, and so an additional 12 runs were conducted to completely populate the design space (gray points).

B. CFD Results and Discussion

The computational simulations were conducted using the commercial software FLUENT, and the computational grids were constructed using FLUENT's grid-generator GAMBIT. All cases were run inviscidly, using FLUENT's coupled implicit solver in conjunction with the advection upstream-splitting-method differencing scheme. The Courant–Friedrichs–Lewy number was set to 1.0. The solutions assumed air as an ideal gas, with a constant ratio of specific heats γ of 1.4. First-order-accurate solutions were generally obtained within 1000 iterations and second-order accuracy generally required an additional 1000 steps on a dual 2.8-GHz processor PC with 2 GB of RAM.

Before running the test matrix, a grid resolution study was conducted. The test case was a $M_{des} = 7$, $CR_{des} = 9.97$, and $\delta_{trunc} = 3$ deg design. As summarized in Table 1, coarse-, moderate-, and fine-mesh grids were evaluated; each successive grid was four times as dense as the preceding case. Note that, as shown in Table 1, the grid size is characterized by the axial distribution times the radial distribution of points. The results of the grid study are also displayed in Table 1 in terms of the time it took the solution to yield a second-order-accurate result, as well as the conservation-averaged pressure ratio, Mach number, and total pressure recovery at the throat. Both of the reduced-size meshes yielded results very similar to the fine-mesh results in significantly less time. In comparison with the fine-mesh solution, the coarse-mesh results fell within 0.2% in pressure ratio, 0.1% in Mach number, and 0.3% in pressure recovery, and the coarse-mesh solution was obtained in 4% of the time. Accordingly, in comparison with the fine-mesh solution, the moderate-density-mesh results fell within 0.1% in terms of pressure ratio, Mach number, and pressure recovery, and the moderate-density-mesh solution was obtained in 20% of the time. It was also of interest in the study to characterize the axial location of the intersection of the bow shock with the centerline, as well as the radial location of the reflected shock at the throat station. Therefore, fairly fine-grid resolution was needed to pinpoint the locations of the shocks at the boundaries of the mesh. Consequently, the moderate-density mesh was chosen because it represented a compromise of run time with grid density and yielded accurate performance results.

Table 1 Grid resolution study results

Grid size	Time, min	PR	M_2	Π
160×50	6	30.159	3.831	0.881
320×100	31	30.197	3.829	0.879
640×200	144	30.222	3.827	0.878

All 27 simulations were performed and the conservation-averaged properties at the throat were obtained. In all but two cases, second-order accuracy was achieved. In the two abnormal runs ($M_{des} = 4$, $CR_{des} = CR_{max}$, and $\delta_{trunc} = 3$ deg and $M_{des} = 4$, $CR_{des} = CR_{max}$, and $\delta_{trunc} = 5$ deg), first-order-accurate solutions were resolved, but when the second-order solutions were initiated, the reflected shock off the centerline went to the strong shock branch and the inlet unstarted. Because these two solutions were not converged to the same level of accuracy as the other cases, they were eliminated from the study.

V. Comparison of the Pressure-Integral Approach with CFD

An example CFD solution for the inviscid Mach number flowfield inside a truncated Busemann inlet is shown at the top of Fig. 6 for a $M_{des} = 6$, $CR_{des} = 7$, and $\delta_{trunc} = 3$ deg design, compared with a pure Busemann design of the same design Mach number and contraction ratio at the bottom. The sharp truncated leading edge generates a bow shock wave that heads toward the centerline of the inlet. As the shock wave progresses toward the centerline, it curves due to the nonideal compression surface created by the truncation process. The shock wave reflects off of the centerline aft of the theoretical location (coordinates [0, 0]) and subsequently passes through the inlet plane just below the inlet shoulder at the throat. The low Mach contours just aft of the centerline shock reflection denote a region in which the shock wave becomes normal, thus reducing the overall total pressure recovery of the inlet. The pure Busemann design, on the other hand, acts as designed, with linear contours all coalescing at the theoretical focus point and the termination shock striking the inlet shoulder at the throat.

The lower half of Fig. 7 compares the theoretical prediction for shock wave shape in the truncated Busemann inlet with the

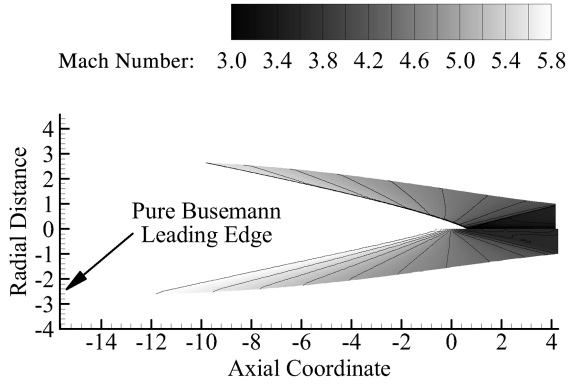

Fig. 6 Example CFD solution for the Mach number in a truncated Busemann inlet (top) and a pure busemann inlet (bottom); $M_{des} = 6$, $CR_{des} = 7$, and $\delta_{trunc} = 3$ deg.

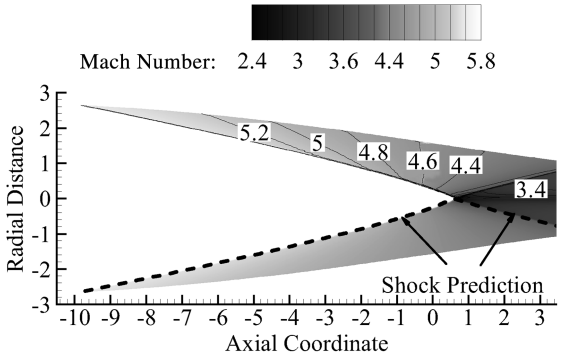

Fig. 7 Example CFD solution for the Mach number in a truncated Busemann inlet and corresponding prediction of shock shape from theory; $M_{des} = 6$, $CR_{des} = 7$, and $\delta_{trunc} = 3$ deg.

computational solution. It is observed that the shock wave curvature for the vast majority of the bow shock wave almost perfectly matches between CFD and theory. It is only near the intersection point at which the theoretical shock begins to diverge, reflecting approximately 0.056 units upstream of the CFD solution. The subsequent reflection shock wave is observed to match well with the CFD prediction, approximately 0.075 units away from the CFD reflection shock wave at the inlet-throat plane. The excellent match in shock wave profile upstream of the shock-reflection location verifies the basic assumptions first imposed in Secs. III.B and III.C.

The CFD solution shown in Fig. 7 was used to find the surface distributions for the Mach number and static pressure ratio. These distributions were then compared with the predictions using the pressure-integral-prediction approach discussed in Sec. III.B. The results are shown in Fig. 8. The profiles show excellent agreement over the vast majority of the inlet, deviating only near the inlet-throat shoulder. This deviation is caused by the characteristics emanating from the highly curved portion of the bow shock near the centerline reflection location. It would thus be expected that as the truncation angle increases and the shock wave gets steeper, the deviation near the throat will become more pronounced and move further upstream.

Comparisons of conservation-averaged performance between theory and CFD are shown in Figs. 9–11 for inlet-throat pressure ratio, inlet-throat Mach number, and inlet-throat total pressure recovery, respectively. The current theory does an excellent job of matching the inlet-throat pressure ratio for moderate truncation angles (3 deg and less), moderate Mach numbers (4 through 7), and moderate contraction ratios (0.65 CR_{max} and less). For the highest truncation angle and contraction ratio, the theory underpredicts the pressure ratio, compared with the CFD results. The same trends are observed for the inlet-throat Mach number, for which moderate truncation angle, Mach number, and contraction ratio yielded excellent agreement, with trends falling off at a high truncation angle

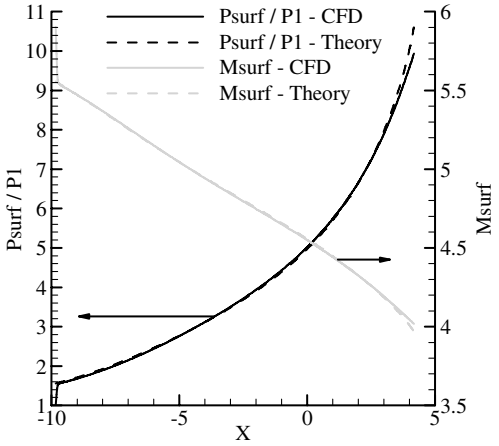

Fig. 8 Comparison of CFD and theoretical surface predictions; $M_{des} = 6$, $CR_{des} = 7$, and $\delta_{trunc} = 3$ deg.

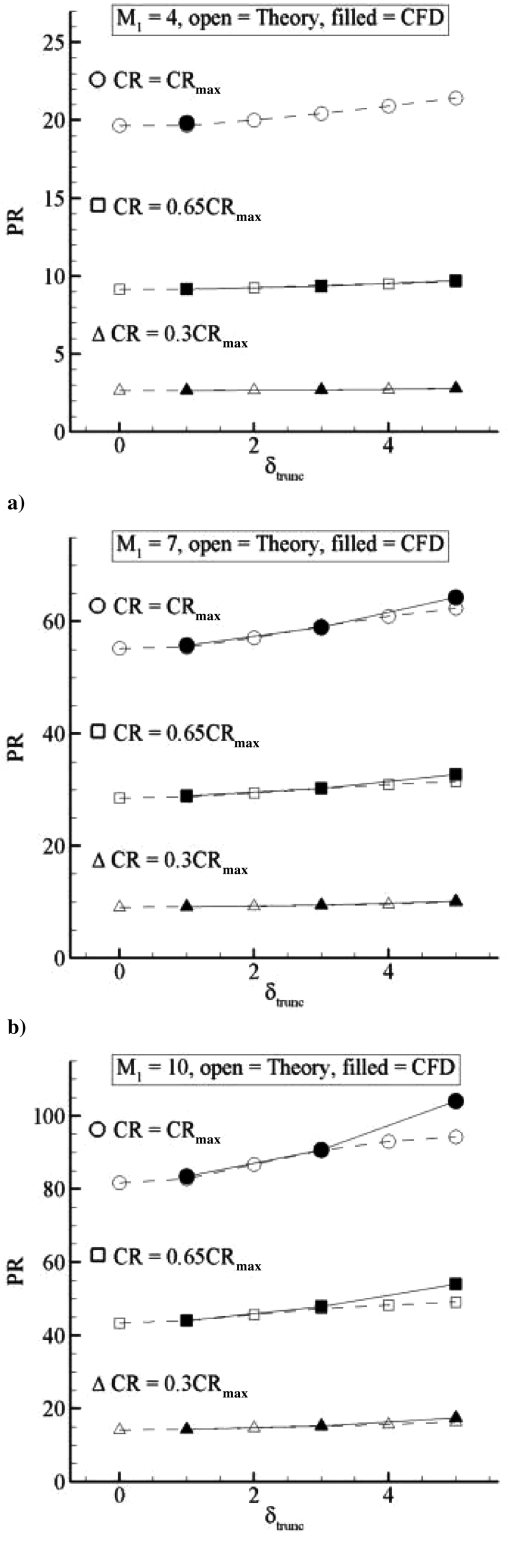

Fig. 9 Conservation-averaged throat pressure ratio: a) 4, b) 7, and c) 10.

and contraction ratio. The results are more mixed when observing the prediction of total pressure recovery. It is noted from Eq. (6) that the total pressure recovery is a very strong function of the inlet-throat Mach number. Hence, even small deviations in the prediction of throat Mach number yield large deviations for total pressure recovery. Again, the same trend is observed, in which the theory well matches the CFD data for moderate truncation angle, Mach number, and contraction ratio.

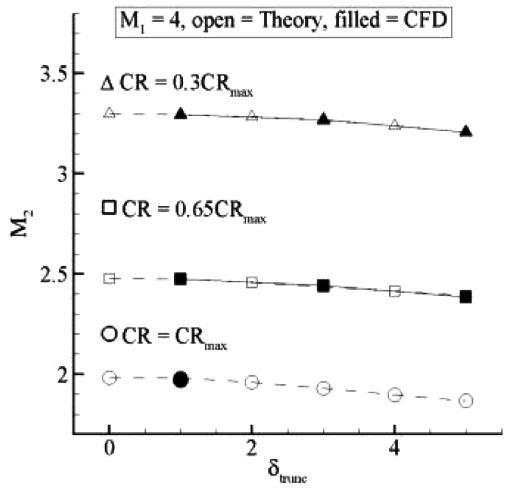

a)

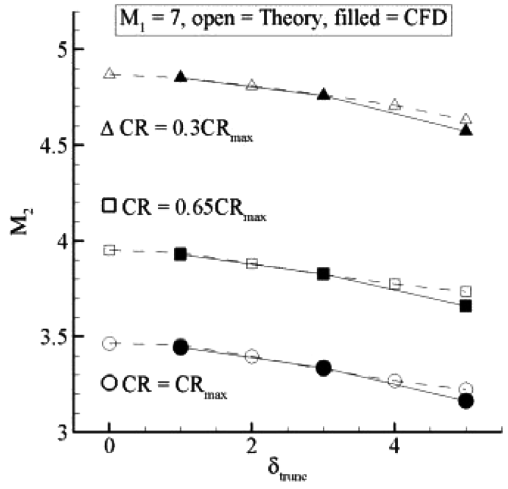

b)

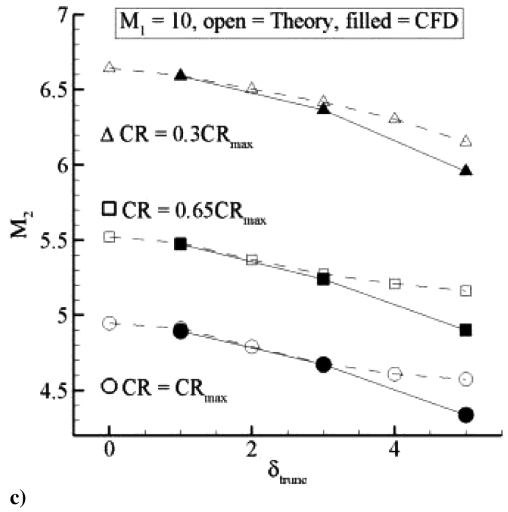

c)

Fig. 10 Conservation-averaged throat Mach number: a) 4, b) 7, and c) 10.

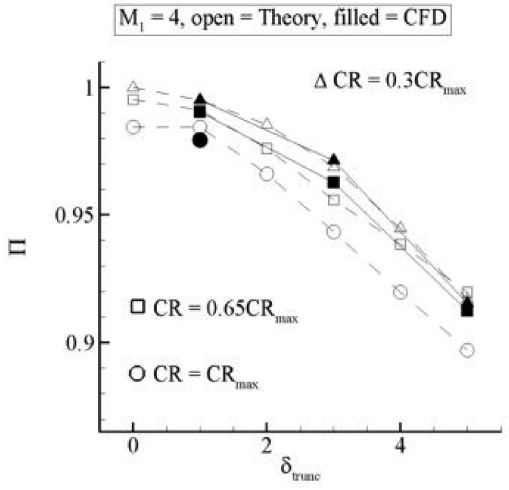

a)

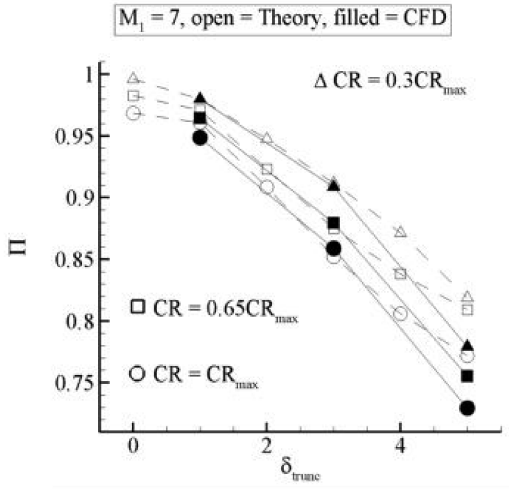

b)

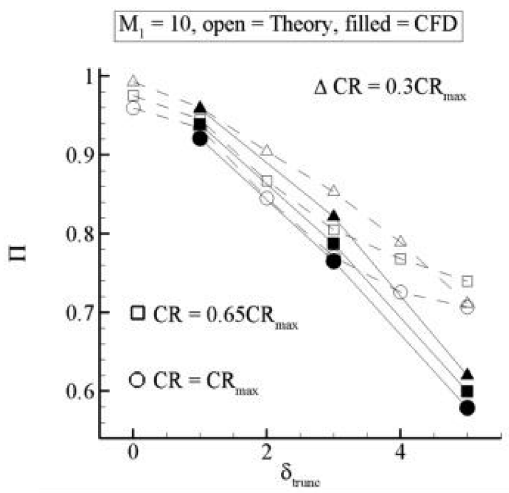

c)

Fig. 11 Conservation-averaged throat total pressure recovery: a) 4, b) 7, and c) 10.

Finally, a comparison is made between the axisymmetric CFD solution, the theoretical shock prediction, and the symmetry plane of a three-dimensional solution on a streamline-traced geometry in Fig. 12. The streamline-traced geometry is a so-called "sugar scoop" design, in which the inlet leading edge and the throat are both circular in cross section. The three-dimensional computational solution validated both that the streamline-tracing approach was correct and that the predicted shock shape within the inlet matched the axisymmetric results.

VI. Conclusions

An analytical approach was presented to predict the Mach number and pressure distribution on a truncated Busemann-inlet surface. The resulting distributions were applied to the conservation equations to calculate the conservation-averaged performance at the inlet-throat plane. The distributions were also applied to predict the bow and terminating shock wave shapes. The analytical results were compared with inviscid CFD solutions solved using the FLUENT

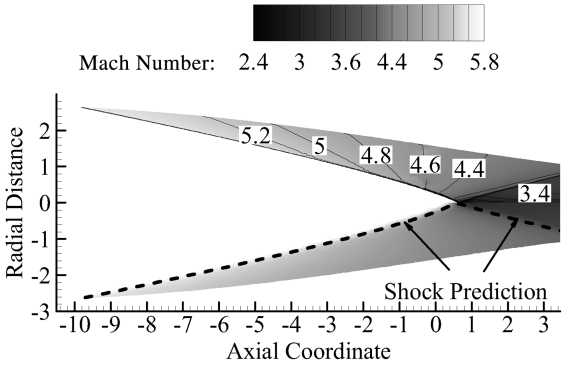

Fig. 12 Example CFD solution for the Mach number in a truncated Busemann inlet (top) and the symmetry plane of a three-dimensional streamline-traced design (bottom); $M_{\text{des}} = 6$, $\text{CR}_{\text{des}} = 7$, and $\delta_{\text{trunc}} = 3$.

code. The results showed good agreement between theory and the computational solutions for inlets of moderate Mach number, truncation angle, and contraction ratio.

The computational results confirmed the key assumptions used in modeling the truncated Busemann-inlet flowfield:

1) The leading-edge conditions can be modeled by an ICFA leading edge that ends at the desired truncation angle.

2) The Mach number and pressure distribution on a truncated Busemann inlet can be modeled from the pure nontruncated Busemann inlet of the same design Mach number and contraction ratio.

3) The truncated Busemann-inlet flowfield can be characterized as being conical, with isobars focusing at the theoretical point of the pure Busemann inlet from which it was derived.

References

[1] Busemann, A., "Die Achsensymmetrishce Kegligle Uberschallstromung," *Luftfahrtforschung*, Vol. 19, 1942, pp. 137–144.

[2] Billig, F. S., Baurle, R. A., Tam, C. J., and Wornom, S. F., "Design and Analysis of Streamline Traced Hypersonic Inlets," 9th International Space Planes and Hypersonic Systems and Technologies Conference, Norfolk, VA, AIAA Paper 99-4974, Nov. 1999.

[3] Billig, F. S., and Kothari, A. P., "Streamline Tracing: Technique for Designing Hypersonic Vehicles," *Journal of Propulsion and Power*, Vol. 16, No. 3, May–June 2000, pp. 465–471.

[4] Billig, F. S., and Jacobsen, L. S., "Comparison of Planar and Axisymmetric Flowpaths for Hydrogen Fueled Space Access Vehicles," 39th AIAA/ASME/SAE/ASEE Joint Propulsion Conference and Exhibit, Huntsville, AL, AIAA Paper 2003-4407, July 2003.

[5] Bulman, M. J., and Siebenhaar, A., "The Rebirth of Round Hypersonic Propulsion," 42nd AIAA/ASME/SAE/ASEE Joint Propulsion Conference and Exhibit, Sacramento, CA, AIAA Paper 2006-5035, July 2006.

[6] Taylor, G. I., and Maccoll, J. W., "The Air Pressure on a Cone Moving at High Speed," *Proceedings of the Royal Society of London, Series A: Mathematical and Physical Sciences*, Vol. 139, 1933, pp. 278–311.

[7] Molder, S., "Internal, Axisymmetric, Conical Flow," *AIAA Journal*, Vol. 5, No. 7, July 1967, pp. 1252–1255.

[8] Molder, S., and Szpiro, E. J., "Busemann Inlet for Hypersonic Speeds," *Journal of Spacecraft and Rockets*, Vol. 3, No. 8, Aug. 1966, pp. 1303–1304.

[9] Molder, S., and D'Souza, N., "Applicability of Hypersonic Small-Disturbance Theory and Similitude to Internal Hypersonic Conical Flows," *Journal of Spacecraft and Rockets*, Vol. 7, No. 2, Feb. 1970, pp. 149–154.

[10] Jacobsen, L., Tam, C., Behdadnia, R., and Billig, F., "Starting and Operation of a High Contraction Ratio Streamline-Traced Busemann Inlet at Mach 4," 42nd AIAA/ASME/SAE/ASEE Joint Propulsion Conference and Exhibit, Sacramento, CA, AIAA Paper 2006-4508, July 2006.

[11] Billig, F. S., "Supersonic Combustion Ramjet Missile," *Journal of Propulsion and Power*, Vol. 11, No. 6, Nov.–Dec. 1995, pp. 1139–1146.

[12] Tam, C.-J., and Baurle, R. A., "Inviscid CFD Analysis of Streamline Traced Hypersonic Inlets at Off-Design Conditions," 39th AIAA Aerospace Sciences Meeting and Exhibit, Reno, NV, AIAA Paper 2001-0675, Jan. 2001.

[13] Tam, C.-J., Baurle, R. A., and Streby, G. D., "Numerical Analysis of Streamline-Traced Hypersonic Inlets," 41st Aerospace Sciences Meeting and Exhibit, Reno, NV, AIAA Paper 2003-13, Jan. 2003.

[14] Baurle, R. A., *Busemann Inlet Design Code*, Taitech, Inc., Beavercreek, OH, 2006.

[15] Lees, L., "Hypersonic Flow," *Fifth International Aeronautical Conference*, Inst. of Aeronautical Sciences, New York, 1955, pp. 241–276.

[16] Billig, F. S., "Shock-Wave Shapes Around Spherical- and Cylindrical-Nosed Bodies," *Journal of Spacecraft and Rockets*, Vol. 4, No. 6, June 1967, pp. 822–823.

[17] White, F. M., *Viscous Fluid Flow*, 2nd ed., McGraw–Hill, Boston, 1991.

[18] Heiser, W. H., and Pratt, D. T., *Hypersonic Airbreathing Propulsion*, 4th Printing, AIAA Education Series, AIAA, Washington, D.C., 1994, pp. 256–257.

F. Liu
Associate Editor